HHS Public Access

Author manuscript

Adv Mater. Author manuscript; available in PMC 2015 October 08.

Published in final edited form as:

Adv Mater. 2014 October 8; 26(37): 6401–6408. doi:10.1002/adma.201400914.

Dye Loaded Ferritin Nanocages for Multimodal Imaging and Photothermal Therapy

Peng Huang,
Laboratory of Molecular Imaging and Nanomedicine (LOMIN), National Institute of Biomedical Imaging and Bioengineering (NIBIB), National Institutes of Health, Bethesda, Maryland 20892, United States

Pengfei Rong,
Laboratory of Molecular Imaging and Nanomedicine (LOMIN), National Institute of Biomedical Imaging and Bioengineering (NIBIB), National Institutes of Health, Bethesda, Maryland 20892, United States

State Key Laboratory for Powder Metallurgy, Central South University, Changsha, Hunan 410083, ChinaDepartment of Radiology, The Third Xiangya Hospital, Central South University, Changsha, Hunan 410013, PR China

Albert Jin,
Laboratory of Cellular Imaging and Macromolecular Biophysics, National Institute of Biomedical Imaging and Bioengineering (NIBIB), National Institutes of Health, Bethesda, Maryland 20892, United States

Xuefeng Yan,
Laboratory of Molecular Imaging and Nanomedicine (LOMIN), National Institute of Biomedical Imaging and Bioengineering (NIBIB), National Institutes of Health, Bethesda, Maryland 20892, United States

Molly Gu Zhang,
Laboratory of Molecular Imaging and Nanomedicine (LOMIN), National Institute of Biomedical Imaging and Bioengineering (NIBIB), National Institutes of Health, Bethesda, Maryland 20892, United States

Jing Lin,
Laboratory of Molecular Imaging and Nanomedicine (LOMIN), National Institute of Biomedical Imaging and Bioengineering (NIBIB), National Institutes of Health, Bethesda, Maryland 20892, United States

Hao Hu,
Laboratory of Molecular Imaging and Nanomedicine (LOMIN), National Institute of Biomedical Imaging and Bioengineering (NIBIB), National Institutes of Health, Bethesda, Maryland 20892, United States

Zhe Wang,

Correspondence to: Peng Huang, peng.huang@nih.gov; Xiaoyuan Chen, shawn.chen@nih.gov.
P. Huang and P. Rong contributed equally to this work

Laboratory of Molecular Imaging and Nanomedicine (LOMIN), National Institute of Biomedical Imaging and Bioengineering (NIBIB), National Institutes of Health, Bethesda, Maryland 20892, United States

Center for Molecular Imaging and Translational Medicine, School of Public Health, Xiamen University, Xiamen 361005, China

Xuyi Yue,
Laboratory of Molecular Imaging and Nanomedicine (LOMIN), National Institute of Biomedical Imaging and Bioengineering (NIBIB), National Institutes of Health, Bethesda, Maryland 20892, United States

Center for Molecular Imaging and Translational Medicine, School of Public Health, Xiamen University, Xiamen 361005, China

Wanwan Li,
Laboratory of Molecular Imaging and Nanomedicine (LOMIN), National Institute of Biomedical Imaging and Bioengineering (NIBIB), National Institutes of Health, Bethesda, Maryland 20892, United States

Gang Niu,
Laboratory of Molecular Imaging and Nanomedicine (LOMIN), National Institute of Biomedical Imaging and Bioengineering (NIBIB), National Institutes of Health, Bethesda, Maryland 20892, United States

Wenbin Zeng,
State Key Laboratory for Powder Metallurgy, Central South University, Changsha, Hunan 410083, China

Wei Wang,
Department of Radiology, The Third Xiangya Hospital, Central South University, Changsha, Hunan 410013, PR China

Kechao Zhou, and
State Key Laboratory for Powder Metallurgy, Central South University, Changsha, Hunan 410083, China

Xiaoyuan Chen
Laboratory of Molecular Imaging and Nanomedicine (LOMIN), National Institute of Biomedical Imaging and Bioengineering (NIBIB), National Institutes of Health, Bethesda, Maryland 20892, United States

Peng Huang: peng.huang@nih.gov; Xiaoyuan Chen: shawn.chen@nih.gov

Keywords

Theranostics; ferritin; IR820; ICG; fluorescence imaging; photoacoustic imaging; photothermal therapy

Activatable theranostics are novel clinical solutions for early recognition, diagnosis, monitoring, and prognosis of diseases by enhancing contrast in various imaging modalities

followed by tailored therapy.[1] Light, typically a wavelength-selected laser, as an exogenous stimulus with the advantage of spatiotemporal selectivity, has been extensively employed for photothermal, photodynamic, and/or photo-triggered chemo/gene therapy.[2] Photothermal therapy (PTT) that employs photothermal conversion agents (PTCAs) to destroy cancer tissues/cells by absorbing and transferring optical laser irradiation energy into heat has been increasingly recognized as a promising minimally invasive alternative to traditional cancer treatments.[2d, 3] Due to the relatively low absorption/scattering of skin, tissue, blood, and water in the transparency window (650~950 nm), near-infrared (NIR) light mediated PTCAs have shown effectiveness in *in vivo* PTT treatment.[4]

A variety of organic/inorganic compounds/nanomaterials, such as indocyanine green (ICG), polyaniline nanoparticles (NPs), polypyrrole NPs, metal NPs (Au, Ag, Pd, and Ge), semiconductor NPs ($Cu_{2-x}Se$ and CuS), carbon-based materials (carbon nanotubes and graphenes), have been widely explored as PTCAs for PTT.[2a, 5] However, most of these PTCAs are nonbiodegradable, immunogenic, with poor pharmacokinetics or potential long-term toxicity, which limit their clinical use.[3b, 6] Therefore, development of novel biodegradable PTCAs with negligible toxicity and immunogenicity, suitable pharmacokinetics, high tumor accumulation rate, and real-time visualization is highly desirable to improve their *in vivo* PTT of cancer.

Indocyanine green (ICG), a FDA-approved NIR dye, owing to its serious photobleaching, short bloodstream circulation half-life and low tumor accumulation rate, is not an effective PTT agent.[7] Recently, NIR dye-loaded micelles have been reported to overcome several above mentioned shortcomings for both NIR fluorescence imaging and PTT.[8] Due to the fact that both fluorescence imaging and phototherapy are strongly dependent on the light excitation wavelength, high fluorescence quantum yield (QY) of the dye is required for fluorescence imaging, at the expense of lowering the photothermal conversion efficiency for PTT. Therefore, the attainment of balance between the dual roles of imaging contrast and photothermal conversion for both optical imaging and PTT is a grand challenge.

Recently, several naturally occurring protein macromolecules have emerged as a novel class of drug delivery vehicles.[9] For example, albumin-based drug delivery systems such as methotrexate-albumin conjugate, albumin-binding prodrug of doxorubicin (DOX), and albumin paclitaxel nanoparticle (Abraxane®) have been evaluated in the clinic.[9] Ferritin (FRT), a major iron storage protein in humans and most living organisms, has also been applied for efficient drug delivery.[10] FRT nanocage is composed of 24 subunits, which self-assemble into a cage-like nanostructure, with external and internal diameters of 12 and 8 nm, respectively. In nature, the internal cavity is suitable for loading different species.[11] We have demonstrated that doxorubicin precomplexed with Cu(II) can be loaded onto RGD modified apoferritin nanocages with high efficiency, and zinc hexadecafluorophthalocyanine ($ZnF_{16}Pc$) can be conveniently encapsulated into RGD4C-modified apoferritins (RFRTs).[10] FRT and its derivatives show great potential as a new type of drug carrier with high loading rates, good tumor selectivity and small particle size. More importantly, FRT as a natural polymer causes fewer concerns than synthetic carriers for clinical translation.

Herein, for the first time, we report a novel “chameleon” theranostic platform based on an NIR dye (new cyanine green, IR820)[12] loaded ferritin (DFRT) nanocages with strong absorbance in the NIR region, due to the strong interaction between IR820 dye and FRT,[13] for photoacoustic/fluorescence multimodal imaging-guided PTT. With separated excitation wavelengths, 550 nm for fluorescence imaging with high fluorescence quantum yield (QY) and 808 nm for photoacoustic imaging (PAI) and PTT with high photothermal conversion efficiency, we successfully achieved simultaneous optimization of dual roles between imaging contrast and photothermal conversion for imaging-guided PTT.

DFRT was formed by ‘opening’ and ‘closing’ the FRT nanocages in the presence of dye molecules. The dye encapsulation was carried out using direct and step-wise change of pH of the solutions from 2 to 7.4.[10, 14] Both FRT and DFRT were characterized similarly by atomic force microscopy (AFM) (Figure 1). Figure 1a and 1b shows the AFM image of the original FRT as well-defined spherical nanoparticles. The 3D AFM image clearly visualizes the protein coats on the surface of FRT in Figure 1b. DFRT appears to be slightly larger and more variable in size than FRT (Figure 1c). As shown in Figure 1d, the diameter of FRT is around 12 nm (determined by AFM measured height), matching the theoretical value, and slight broadening in the X-Y direction due to nanoparticle compression and AFM-tip size. Histogram distribution of the equivalent spherical diameter ($(6V/\pi)^{1/3}$) for the FRT and DFRT nanoparticles shown in Figure 1e indicate significant loading of IR820 dye molecules.

Next we investigated the photophysical and photochemical properties of DFRT using optical absorption and fluorescence spectra. Figure 2a and Figure S1 showed UV-Vis absorbance spectra of FRT, IR820 dye, and DFRT. The IR820 dye exhibits a strong peak at 687 nm, and a weak shoulder at 825 nm. FRT without dye shows virtually no absorption in the range of 500 ~ 900 nm. After the dye is loaded into FRT, DFRT exhibits a weak shoulder at 761 nm, and a strong peak at 835 nm. The remarkably red-shifted absorption may be attributed to the strong interaction between dye and FRT. The loading process is accompanied with a color change of the solution from dark green to brown (Figure S2a). The absorption spectrum of DFRT is different from that of unloaded IR820 dye (Figure S2b–d). With different mole ratios of ferritin and IR820 such as 1:50, 1:80, and 1:100, the IR820 loading efficiencies were 17.32, 25.11, and 29.53 wt%, respectively. We chose the mole ratio of 1:50 for the remaining experiments.

The fluorescence excitation spectrum of IR820 dye shows the two excitation wavelengths at 550 and 770 nm, respectively (Figure S3). As shown in Figure 2b, both IR820 dye and DFRT exhibited a shift in emission peaks from 604 nm to 834 nm as the excitation wavelength was changed from 550 nm to 770 nm. The results also show fluorescence quenching, most likely owing to the tight packing of IR820 dye molecules after being loaded into FRT. The quenching efficiency of IR820 dye in DFRT upon 550 nm excitation is ~20%, but almost ~80% upon 770 nm excitation. Based on these results, we selected 550 nm for fluorescence imaging with high fluorescence QY and 808 nm for PTT with high photothermal conversion efficiency. Upon separated excitation wavelengths, the dual roles of DFRT between contrast agent and PTCA are easy to alternate for imaging and PTT.

To further verify the red-shifted absorption and fluorescence quenching of dye loaded FRT, we chose ICG, a FDA-approved NIR dye, for comparison. The similar results were observed in Figure S4. ICG has a strong peak at 683 nm, and a weak shoulder at 780 nm. After being encapsulated into FRT, ICG-FRT exhibits a weak shoulder at 725 nm, and a strong peak at 800 nm. The loading process is also accompanied by a color change of the solution from light green to black (Figure S2). A marked fluorescence quenching of ICG upon 760 nm excitation was found after FRT loading. Interestingly, there is ~4.5 fold fluorescence enhancement of ICG at 700 nm emission peak upon 630 nm excitation in ICG-FRT system. Therefore, the ICG-FRT is also suitable for simultaneous optimization of imaging and PTT using separated wavelengths, 630 nm for fluorescence imaging with high fluorescence QY and 808 nm for PAI and PTT with high photothermal conversion efficiency. These results suggest the great potential of FRT as a new type of carrier for dye delivery, fluorescence and PA imaging, and enhanced PTT treatment.

We next studied the potential of DFRT in PTT of cancer by measuring the temperature elevation of FRT, IR820 dye, and DFRT in aqueous solutions exposed to an 1 W/cm^2 808 nm laser for 5 min (Figure 2c). No obvious temperature change was observed in the control group of pure FRT, due to the lack of absorption of FRT in the range of 500 ~ 900 nm. Upon same laser exposure, IR820 dye and DFRT (80 μg/mL of dye) raised the temperature by 18.34 and 28.38 °C, respectively. These results suggest significantly higher photothermal conversion efficiency of DFRT over the IR820 dye upon 808 nm excitation. The effective photothermal conversion also supports the use of DFRT for PAI[15] (Figure 2d). The best excitation wavelength range is from 800 to 850 nm. To achieve *in vivo* simultaneous PAI and PTT, we chose 808 nm as the excitation wavelength for PAI.

Encouraged by high photothermal conversion efficiency of DFRT upon 808 nm excitation, we next investigated *in vitro* PTT efficacy and cytotoxicity of DFRT. Live/dead cells were differentiated by Calcein AM (live cells, green fluorescence) and propidium iodide (PI) (dead cells, red fluorescence) co-staining after PTT treatment (Figure 3a). In the control groups (IR820 dye or DFRT only), all the cells displayed green fluorescence, so IR820 dye or DFRT has no measurable cytotoxicity. Upon laser irradiation at different power densities, both IR820 dye and DFRT show laser dose-dependent PTT effect on 4T1 cells. All cells were killed after being incubated with DFRT (50 μg/mL of IR820 dye) and exposed to the NIR laser at 1 W/cm^2 for 5 min. As shown in Figure S5, on the boundary of the laser spot, only cells within the laser spot were killed, showing the intense homogeneous red fluorescence. The cells outside the region of the laser spot stayed alive, showing strong green fluorescence.

To further evaluate the cytotoxicity and PTT efficacy of DFRT, the viability of 4T1 cells after being exposed to various concentrations of DFRT for 24 h without laser irradiation were assessed (Figure 3b). We found DFRT exhibited negligible toxicity at all the test concentrations. Even with 400 μg/mL of DFRT, the cell viability is over 90%, which suggests that DFRT alone has negligible adverse effect on tumor cells. To verify the improved PTT efficacy induced by DFRT, three groups including FRT, IR820 dye and DFRT were compared at the same conditions with increasing laser power. For FRT group, no PTT effect was observed at all studied laser power densities. Upon laser irradiation, both

IR820 dye and DFRT induced a laser dose-dependent cytotoxicity to 4T1 cells, which was significantly different from that of control groups as shown in Figure 3c. DFRT exhibited a much better PTT efficacy than IR820 dye under the same conditions, which is attributed to high photothermal conversion efficiency of DFRT over IR820 dye. The above results are in good agreement with live/dead cell staining results.

To investigate the stability of DFRT at the cellular level, we prepared the FITC-conjugated Cy5.5 loaded FRT (FITC-FRT-Cy5.5). FITC was covalently coupled to primary amines of FRT. Cy5.5 was loaded by FRT using the same method. After 6 h incubation of FITC-FRT-Cy5.5 with 4T1 cells, then we used LysoTracker to stain lysosome and observed FITC-FRT-Cy5.5 using a confocal laser scanning microscopy (CLSM). Figure S6 clearly showed the blue fluorescence signals from Lysotracker match well with the fluorescence signals from FITC-FRT (green) and Cy5.5 (red), suggesting FITC-FRT and Cy5.5 colocalized within the lysosomes. These results indicate FITC-FRT-Cy5.5 is stable in lysosome within 6 h incubation. It would be reasonable to believe that DFRT is also stable in lysosome.

We next investigated the feasibility of using DFRT for *in vivo* multimodal imaging-guided PTT. To achieve the simultaneous optimization of NIR fluorescence and PA imaging, we used the separated wavelengths to excite DFRT, 550 nm for fluorescence imaging with high fluorescence QY and 808 nm for PAI with high photothermal conversion efficiency. Nude Mice with subcutaneous 4T1 tumors were selected as the animal model. When the tumors reached 60 mm^3, the mice were treated with intravenous injection of DFRT (2 mg/mL of IR820 dye, 200 μL). NIR fluorescence imaging was employed to monitor the pharmacokinetics of DFRT *in vivo*. As shown in Figure 4a, distributed DFRT fluorescence was found over the whole body at early time points after injection. With time, the whole body signal gradually decreased and the tumor signal increased. The tumor can be easily differentiated from the surrounding normal tissue with good contrast from 4 to 24 h post-injection. At the 24 h time point, the major organs of unloaded dye or DFRT injected mice were harvested for *ex vivo* imaging (Figure 4b). Meanwhile, the PAI was also used to observe the PA signal change in tumor tissues. Figure 4c shows the snapshots of *in vivo* two dimensional (2D) and 3D cross section ultrasonic (US) and PA images upon 808 nm excitation of tumor area after intravenous injection of IR820 dye or DFRT in mice at multiple time points. The gradual increase of PA signals was observed in the tumor regions of DFRT treated mice.

DFRT accumulation in the tumor was quantified by dye fluorescence intensity (Figure 4d). The average fluorescence intensity from dye acquired in the tumor areas quickly arose within 1~4 h post-injection and reached a plateau during 4~24 h post-injection followed by slight decrease over time. Meanwhile, the quantification of tissues/organs distribution was carried on *ex vivo* imaging (Figure 4E). The relative uptake efficiency (10.48 ± 0.93 %) of DFRT is ~4-fold higher than that of IR820 dye (2.64 ± 0.20 %), which suggested that FRT carrier significantly improved the tumor accumulation rate of dye. The strong fluorescence signals in the liver and spleen may be attributed to the macrophage clearance of IR820 dye and DFRT from blood. Strong kidney signals imply renal clearance of IR820 dye and DFRT. Semi-quantification of PA signals in the tumor area revealed that the average tumor PA intensity (0.95 ± 0.01 a.u.) of DFRT was ~2.6-fold stronger than that of IR820 dye (0.37

± 0.02 a.u.) (Figure 4f), which further confirm that FRT carrier can significantly improve tumor accumulation of the dye molecules. The color of tumor tissue turned dark with increased accumulation of DFRT at late time points after intravenous injection (Figure S7).

Based on effective DFRT-induced PTT *in vitro* and high tumor accumulation rate of DFRT *in vivo*, the *in vivo* PTT studies were carried out on the same animal model. According to the observation from fluorescence and PA imaging, the most suitable time point to implement PTT is at 24 h postinjection of DFRT. Upon 808 nm laser irradiation, thermal imaging was employed to monitor the temperature change *in vivo* using an infrared (IR) thermal camera (Figure 5a and c). For mice injected with DFRT, the tumor temperature changes were 23.8 or 42.2 °C within 10 min, upon 0.5 or 1 W/cm^2 808 nm laser irradiation, respectively. No significant temperature rise was observed in other body parts of the mice (Figure S8). In contrast, upon 1 W/cm^2 808 nm laser irradiation, the local temperature changes of tumors treated with PBS or IR820 dye were increased by about 7.2 or 11.1 °C, respectively. Figure 5b shows 3D color Doppler images of tumor before and after PTT treatment. While the tumor displayed clear blood flow prior to the treatment, no blood flow was observed in the tumor after, which can be attributed to the destruction of the blood vessels of tumor tissue during treatment.

For *in vivo* DFRT-induced PTT treatment, eight groups of 4T1 tumor-bearing mice (4–6 mice/group) were designated as follows: untreated mice (control, n = 6), mice with PBS administration and laser irradiation (PBS + Laser, n = 6), mice with FRT administration but no laser irradiation (FRT, n = 4), mice with FRT administration and laser irradiation (FRT + Laser, n = 4), mice with dye administration but no laser irradiation (IR820 dye, n = 4), mice with dye administration and laser irradiation (IR820 dye + Laser, n = 5), mice with DFRT administration but no laser irradiation (DFRT, n = 4), and mice with DFRT administration and laser irradiation (DFRT + Laser, n = 6). The same 808 nm laser density (0.5 W/cm^2) and exposure time (10 min) was applied in all eight treatments. While the tumors in the control groups all grew at similar speeds, the tumors in both the IR820 dye/laser and DFRT/laser groups exhibited remarkable delay in tumor growth or tumor regression after two weeks (IR820 dye/laser vs. Ctl, $P < 0.05$; DFRT/laser vs. Ctl, $P < 0.001$) (Figure 5d). In the DFRT + laser group, all the tumors were effectively ablated, leaving scars at their original sites without showing reoccurrence (Figure S9). Additionally, it is also worth noting that the DFRT group exhibited significantly higher PTT therapeutic efficacy than the IR820 dye/laser group on day 14 (DFRT/laser vs. IR820 dye/laser, $P < 0.0001$). As shown in Figure 5e, DFRT administration and laser irradiation greatly prolonged mice survival over 40 days, without a single death or tumor reoccurrence. In contrast, for the IR820 dye/laser group, all the mice had to be sacrificed on day 20 due to the extensive tumor burden. Mice in other control groups showed average life spans of ~14 days since treatment started. Hematoxylin and eosin (H&E) staining of tumor sections were collected from four laser irradiation groups of mice at 2 h after laser irradiation (Figure 5f). For the PBS/laser and FRT/laser groups, the histological section showed observable errhysis and an infiltration of small number of inflammatory cells without tissue structure damage. For the IR820 dye/laser group, inflammatory cell infiltration, cell death and errhysis with partial tissue structure damage was observed. For the DFRT/laser group, similar (results) were observed; however, instead

of errhysis with partial tissue structure damage, serious tissue structure damage was (detected). In the high resolution H&E images (Figure S10), we found significant cancer cell damage with nuclear membrane fragmentation and nuclei shrinkage with karyorrhexis and pyknosis in the DFRT/laser group. The irreversible condensation of chromatin and karyorrhexis in the nuclei of tumor cells led to intensive necrosis or apoptosis. The results indicated that the *in vivo* PTT therapeutic efficacy of DFRT was significantly higher than that of IR820 dye.

Furthermore, no significant body weight variation was noticed after DFRT-induced PTT treatment (Figure S11). After DFRT administration and laser irradiation, main organs from different groups of mice, as seen through H&E stained images (Figure S12), showed no obvious damage or inflammation. In accordance with the fact that DFRT has low cytotoxicity and immunogenicity, it is valid to surmise that circulating DFRT does not induce discernable toxic side effects to treated animals. Thus, due to its excellent theranostic capability without noticeable toxicity and immunogenicity, DFRT is a suitable candidate for multimodal imaging-guided PTT *in vivo*.

The following may be considered in future applications of DFRT for cancer theranostics: 1) control of the arrangement of dye molecules inside FRT; 2) precise control of the size of DFRT; 3) enhanced knowledge of the stability of DFRT *in vivo*; 4) modification of the surface of FRT with specific biomarkers to further improve the tumor accumulation rate of DFRT; 5) systematic assessment of the toxicity, biocompability, immunogenicity, pharmacokinetics, and biodistribution of DFRT *in vivo*.

In summary, we have developed a near-infrared dye IR820 loaded ferritin (DFRT) nanocage with strong absorbance in the NIR region for simultaneous fluorescence/photoacoustic/photothermal multimodal imaging-guided enhanced photothermal therapy (PTT). Using separated wavelengths excitation, 550 nm for fluorescence imaging with high fluorescence quantum yield and 808 nm for PAI and PTT with high photothermal conversion efficiency, the optimization of both imaging and PTT is achieved in our system. The cancer theranostic capability using DFRT was carefully investigated both *in vitro* and *in vivo*. Most intriguingly, 100% *in vivo* tumor elimination is achieved by intravenous injection of DFRT, under a low laser power density of 0.5 W/cm^2 without weight loss, tumor recurrence and noticeable toxicity. This concept of protein-based theranostics can potentially be applied for clinical translation of personalized nanomedicine with targeted dye/drug delivery, diagnosis, and treatment.

Supplementary Material

Refer to Web version on PubMed Central for supplementary material.

Acknowledgments

This work was supported by the National Key Basic Research Program (973 Project) (2010CB933901, 2013CB733802, 2014CB744503), the National Science Foundation of China (81272987, 31170961, 51102258, 81371596), and the Intramural Research Program (IRP) of the NIBIB, NIH.

References

1. a) Lovell JF, Jin CS, Huynh E, Jin H, Kim C, Rubinstein JL, Chan WCW, Cao W, Wang LV, Zheng G. Nat Mater. 2011; 10:324–332. [PubMed: 21423187] b) Rai P, Mallidi S, Zheng X, Rahmanzadeh R, Mir Y, Elrington S, Khurshid A, Hasan T. Adv Drug Deliver Rev. 2010; 62:1094–1124.c) Huang P, Lin J, Wang X, Wang Z, Zhang C, He M, Wang K, Chen F, Li Z, Shen G. Adv Mater. 2012; 24:5104–5110. [PubMed: 22718562] d) Lovell JF, Liu T, Chen J, Zheng G. Chem Rev. 2010; 110:2839–2857. [PubMed: 20104890]
2. a) Zhang Z, Wang J, Chen C. Adv Mater. 2013; 25:3869–3880. [PubMed: 24048973] b) Kuo WS, Chang CN, Chang YT, Yang MH, Chien YH, Chen SJ, Yeh CS. Angew Chem Int Ed. 2010; 122:2771–2775.c) Huang P, Xu C, Lin J, Wang C, Wang X, Zhang C, Zhou X, Guo S, Cui D. Theranostics. 2011; 1:240–250. [PubMed: 21562631] d) Huang P, Bao L, Zhang C, Lin J, Luo T, Yang D, He M, Li Z, Gao G, Gao B. Biomaterials. 2011; 32:9796–9809. [PubMed: 21917309] e) Lin J, Wang S, Huang P, Wang Z, Chen S, Niu G, Li W, He J, Cui D, Lu G. ACS Nano. 2013; 7:5320–5329. [PubMed: 23721576] f) Huang P, Lin J, Wang S, Zhou Z, Li Z, Wang Z, Zhang C, Yue X, Niu G, Yang M. Biomaterials. 2013; 34:4643–4654. [PubMed: 23523428] g) Wang S, Huang P, Nie L, Xing R, Liu D, Wang Z, Lin J, Chen S, Niu G, Lu G. Adv Mater. 2013; 25:3055–3061. [PubMed: 23404693] h) Jang B, Choi Y. Theranostics. 2012; 2:190. [PubMed: 22375157]
3. a) Zeng J, Goldfeld D, Xia Y. Angew Chem Int Ed. 2013; 52:4169–4173.b) Huang P, Lin J, Li W, Rong P, Wang Z, Wang S, Wang X, Sun X, Aronova M, Niu G, Leapman RD, Nie Z, Chen X. Angew Chem Int Ed. 2013; 52:13958–13964.
4. a) Wang Y, Black KC, Luehmann H, Li W, Zhang Y, Cai X, Wan D, Liu SY, Li M, Kim P. ACS Nano. 2013; 7:2068–2077. [PubMed: 23383982] b) Yang K, Xu H, Cheng L, Sun C, Wang J, Liu Z. Adv Mater. 2012; 24:5586–5592. [PubMed: 22907876]
5. a) Zha Z, Wang J, Qu E, Zhang S, Jin Y, Wang S, Dai Z. Sci Rep. 2013; 3:2360. [PubMed: 23912977] b) Tian Q, Hu J, Zhu Y, Zou R, Chen Z, Yang S, Li RW, Su Q, Han Y, Liu X. J Am Chem Soc. 2013; 135:8571–8577. [PubMed: 23687972] c) Tian Q, Jiang F, Zou R, Liu Q, Chen Z, Zhu M, Yang S, Wang J, Wang J, Hu J. ACS Nano. 2011; 5:9761–9771. [PubMed: 22059851] d) Tian Q, Tang M, Sun Y, Zou R, Chen Z, Zhu M, Yang S, Wang J, Wang J, Hu J. Adv Mater. 2011; 23:3542–3547. [PubMed: 21735487] e) Hessel CM, Pattani VP, Rasch M, Panthani MG, Koo B, Tunnell JW, Korgel BA. Nano Lett. 2011; 11:2560–2566. [PubMed: 21553924] f) Huang P, Rong P, Lin J, Li W, Yan X, Zhang M, Nie L, Niu J, Lu J, Wang W, Chen X. J. Am. Chem. Soc. 2014; 136:8307–8313. [PubMed: 24842342] g) Shen H, Zhang L, Liu M, Zhang Z. Theranostics. 2012; 2:283. [PubMed: 22448195]
6. Zha Z, Deng Z, Li Y, Li C, Wang J, Wang S, Qu E, Dai Z. Nanoscale. 2013; 5:4462–4467. [PubMed: 23584573]
7. a) Zha Z, Yue X, Ren Q, Dai Z. Adv Mater. 2012; 25:777–782. [PubMed: 23143782] b) Zheng C, Zheng M, Gong P, Jia D, Zhang P, Shi B, Sheng Z, Ma Y, Cai L. Biomaterials. 2012; 33:5603–5609. [PubMed: 22575835]
8. a) Zheng M, Yue C, Ma Y, Gong P, Zhao P, Zheng C, Sheng Z, Zhang P, Wang Z, Cai L. ACS nano. 2013; 7:2056–2067. [PubMed: 23413798] b) Yue C, Liu P, Zheng M, Zhao P, Wang Y, Ma Y, Cai L. Biomaterials. 2013; 34:6853–6861. [PubMed: 23777910] c) Cheng L, He W, Gong H, Wang C, Chen Q, Cheng Z, Liu Z. Adv Funct Mater. 2013; 23:5893–5902.d) Wan Z, Mao H, Guo M, Li Y, Zhu A, Yang H, He H, Shen J, Zhou L, Jiang Z. Theranostics. 2014; 4:399–411. [PubMed: 24578723]
9. Todd TJ, Zhen Z, Xie J. Nanomedicine. 2013; 8:1555–1557. [PubMed: 24074382]
10. a) Zhen Z, Tang W, Chen H, Lin X, Todd T, Wang G, Cowger T, Chen X, Xie J. ACS Nano. 2013; 7:4830–4837. [PubMed: 23718215] b) Zhen Z, Tang W, Guo C, Chen H, Lin X, Liu G, Fei B, Chen X, Xu B, Xie J. ACS Nano. 2013; 7:6988–6996. [PubMed: 23829542]
11. a) Lin X, Xie J, Niu G, Zhang F, Gao H, Yang M, Quan Q, Aronova MA, Zhang G, Lee S. Nano Lett. 2011; 11:814–819. [PubMed: 21210706] b) Lin X, Xie J, Zhu L, Lee S, Niu G, Ma Y, Kim K, Chen X. Angew Chem Int Ed. 2011; 123:1607–1610.
12. Fernandez-Fernandez A, Manchanda R, Lei T, Carvajal DA, Tang Y, Kazmi SZR, McGoron AJ. Mol Imaging. 2012; 11:99–113. [PubMed: 22469238]

13. Gao F, Lin Y, Li L, Liu Y, Mayerhöffer U, Stolte M, Su J, Li J, Würthner F, Wang H. Biomaterials. 2014; 35:1004–1014. [PubMed: 24169004]
14. Kilic MA, Ozlu E, Calis S. J Biomed Nanotechnol. 2012; 8:508–514. [PubMed: 22764421]
15. a) Shah J, Park S, Aglyamov S, Larson T, Ma L, Sokolov K, Johnston K, Milner T, Emelianov SY. J Biomed Opt. 2008; 13:034024. [PubMed: 18601569] b) Pramanik M, Wang LV. J Biomed Opt. 2009; 14:054024. [PubMed: 19895126]

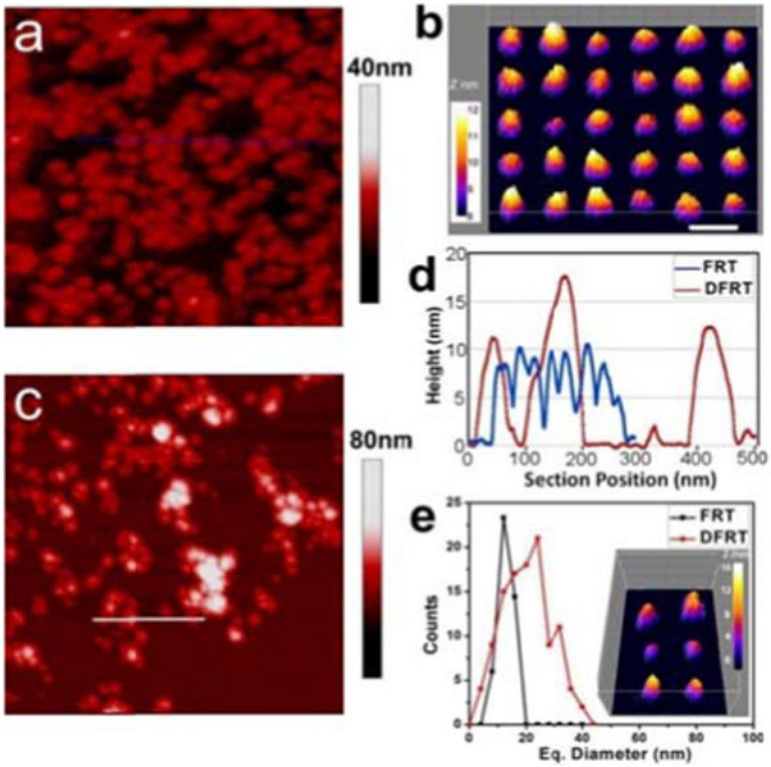

Figure 1.

(a) Topological image of FRT in partial layer coverage on mica surface with 40 nm color-scale for the height. (b) Selected FRT nanocages are presented on a 20 nm grid in 3D to visualize protein coats with color-scale from 8–12 nm in the insert. (c) A representative AFM image of DFRT on mica surface with 80 nm color-scale for the height. (d) Section plot along the blue line in (a) and white line in (c), showing DFRT are larger and more variable in size. (e) Histogram distribution of the equivalent spherical (Eq.) diameter (Eq. Diameter = $(6V/\pi)^{1/3}$) for the FRT and DFRT nanoparticles, showing significant loading of the dye. inset: 3D visualization of DFRT nanoparticles placed on a 100 nm grid.

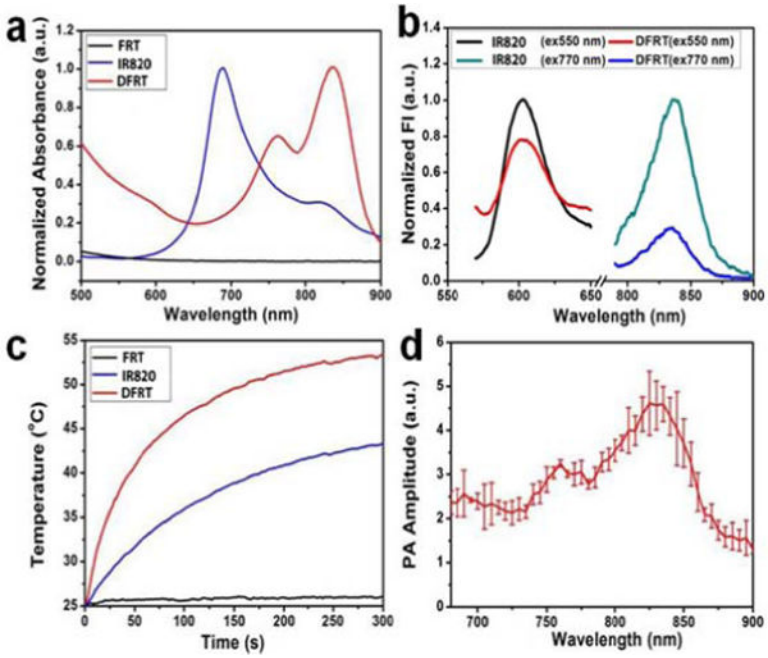

Figure 2. Characterization of DFRT

(a) UV-Vis absorbance spectra of FRT, IR820 dye, and DFRT. (b) Fluorescence emission spectra of IR820 dye and DFRT. (c) Temperature elevation of aqueous solution samples with same concentration as a function of irradiation time and (d) Photoacoustic (PA) spectrum of DFRT.

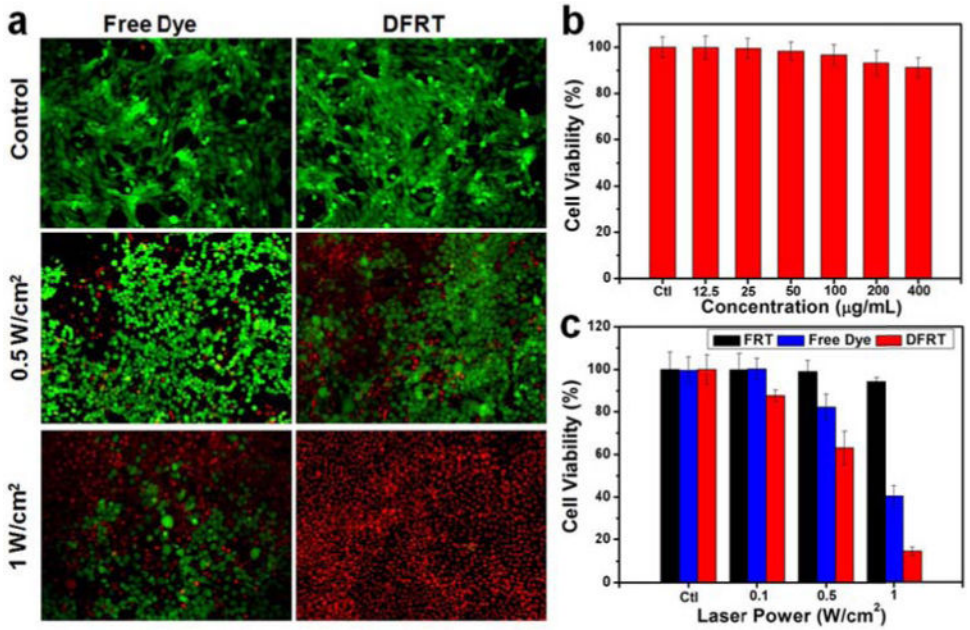

Figure 3. ***In vitro*** **cell experiments**

(a) Fluorescence images of Calcein AM/PI co-stained 4T1 cells with free IR820 dye or DFRT (50 μg/mL dye) incubation for 6 h after being exposed to the 808 nm laser at different power densities of 0.5 and 1 W/cm^2 for 5 min. The cells incubated with same concentration of free IR820 dye or DFRT without laser irradiation were chosen as control. (b) Viability of 4T1 cells after being incubated with various concentrations of DFRT for 24 h. (c) Viabilities of 4T1 cells after DFRT-induced photothermal therapy at different laser power densities. Cell viability was normalized to the control group without any treatment. Error bars were based on the standard deviations of five parallel samples.

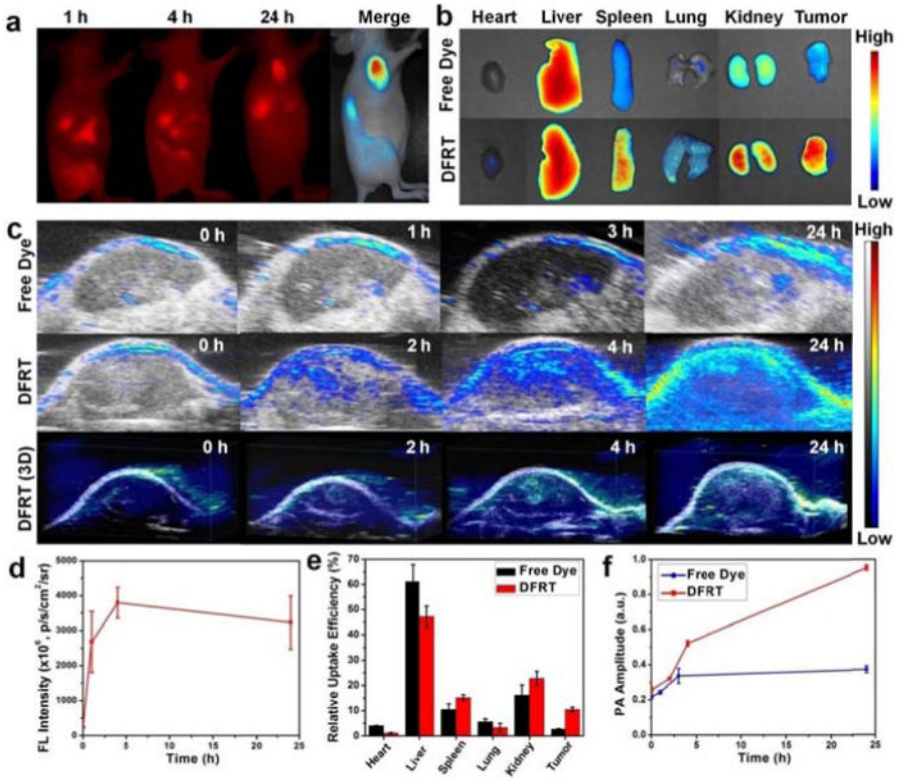

Figure 4. *In vivo* NIR fluorescence (FL) and photoacoustic (PA) imaging

(a) *In vivo* NIR FL images after intravenous injection of DFRT in mice at different time points; (b) *ex vivo* NIR FL images of mouse tissues (from left to right: heart, liver, spleen, lung, kidneys, tumor), harvested at a 24 h time point post-injection of free IR820 dye or DFRT. (c) *In vivo* two dimensional (2D) and 3D cross-section ultrasonic (US) and PA images of tumor tissues after intravenous injection of free IR820 dye or DFRT in mice at different time points. (d) Time-lapse FL signal change of tumors followed by intravenous injection of DFRT. (e) Biodistribution of free IR820 dye or DFRT in 4T1 tumor-bearing nude mice at 24 h post-injection. (f) Time-lapse PA signal change of tumors followed by intravenous injection of free IR820 dye or DFRT. (mean ± standard deviation; n = 3 per group)

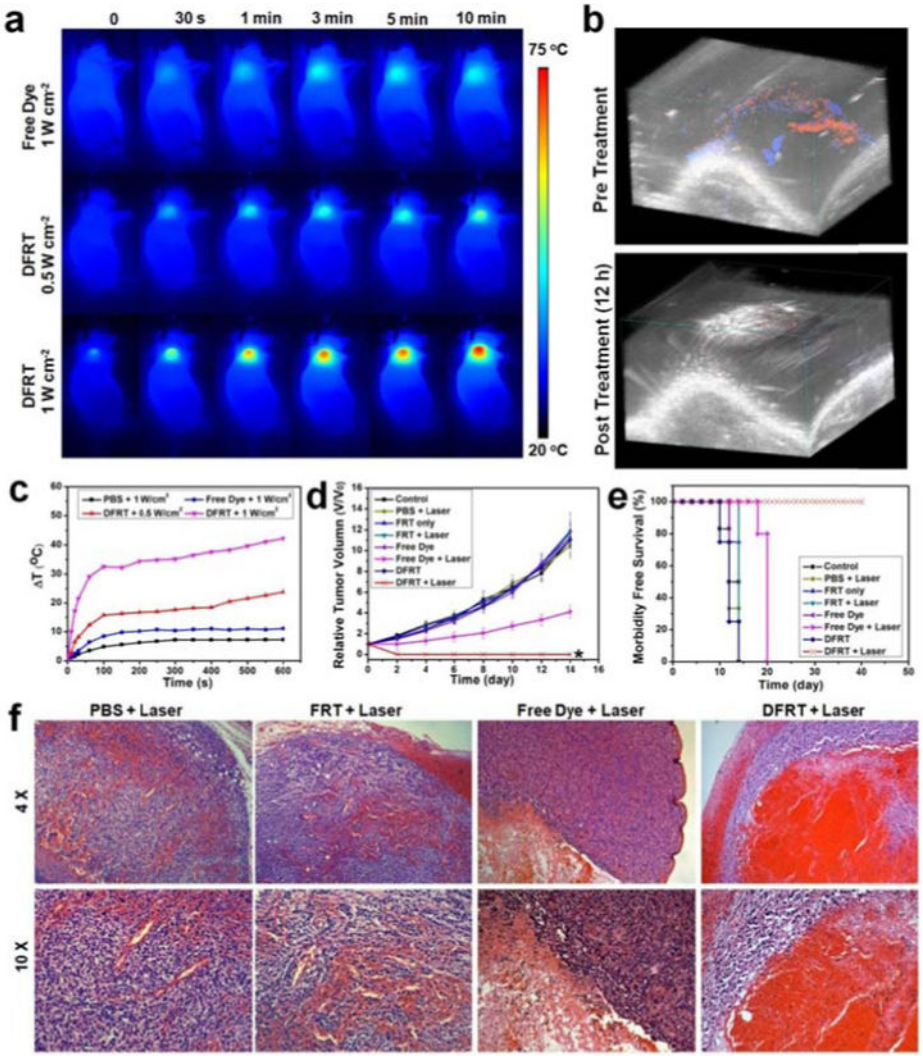

Figure 5. ***In vivo*** **photothermal therapy**

(a) Thermal images of 4T1 tumor-bearing mice with injection of free IR820 dye or DFRT and exposure to 808 nm laser. (b) 3D color Doppler images of tumor before and 12 h after PTT treatment. (c) Heating curves of 4T1 tumors upon laser irradiation as a function of irradiation time. (d) Tumor growth curves of different groups of 4T1 tumor-bearing mice after treatment. Tumor volumes were normalized to their initial sizes. Error bars represent the standard deviations of 4–6 mice per group. * $P < 0.01$. (e) Survival curves of tumor-bearing mice after various treatments. DFRT injected mice after PTT treatment showed 100% survival over 40 days. (f) H&E staining of tumor sections collected from different groups of mice at 2 h after laser irradiation.